

Graph Attention-based Decentralized Actor-Critic for Dual-Objective Control of Multi-UAV Swarms

Haoran Peng, *Member, IEEE*, and Ying-Jun Angela Zhang, *Fellow, IEEE*

Abstract—This research focuses on optimizing multi-UAV systems with dual objectives: maximizing service coverage as the primary goal while extending battery lifetime as the secondary objective. We propose a Graph Attention-based Decentralized Actor-Critic (GADC) to optimize the dual objectives. The proposed approach leverages a graph attention network to process UAVs' limited local observation and reduce the dimension of the environment states. Subsequently, an actor-double-critic network is developed to manage dual policies for joint objective optimization. The proposed GADC uses a Kullback-Leibler (KL) divergence factor to balance the tradeoff between coverage performance and battery lifetime in the multi-UAV system. We assess the scalability and efficiency of GADC through comprehensive benchmarking against state-of-the-art methods, considering both theory and experimental aspects. Extensive testing in both ideal settings and NVIDIA Sionna's realistic ray tracing environment demonstrates GADC's superior performance.

Index Terms—Unmanned aerial vehicle, graph attention network, multi-agent reinforcement learning.

I. INTRODUCTION

Conventional uncrewed aerial vehicle (UAV) systems rely on direct connections between UAVs and ground user terminals (UTs). This architecture is inherently limited by the communication range and battery capacity of the UAVs [1], [2]. The limited communication range results in localized observation and non-uniform service coverage [3]. As shown in Fig. 1, UAVs handling heavy service loads experience rapid energy depletion, significantly reducing the multi-UAV network's operational lifetime [3], defined as the duration until the first UAV exhausts its power [4]. This challenge necessitates the development of a multi-UAV navigation strategy with dual objectives: maximizing the UAV coverage as the primary objective and prolonging the UAV network lifetime as the secondary objective [1]. In particular, maximum coverage navigation aims to maximize the number of UTs covered across all time steps. Likewise, maximum lifetime navigation aims to equalize residual onboard energy across UAVs, accounting for the UAVs' movement, UAV-UAV communications, and UAV-UTs service loads.

Optimizing the dual objectives—maximizing UAV coverage while extending UAV network lifetime—requires careful management of their inherent trade-offs. Meanwhile, the decentralized nature of UAVs presents the challenge in acquiring global

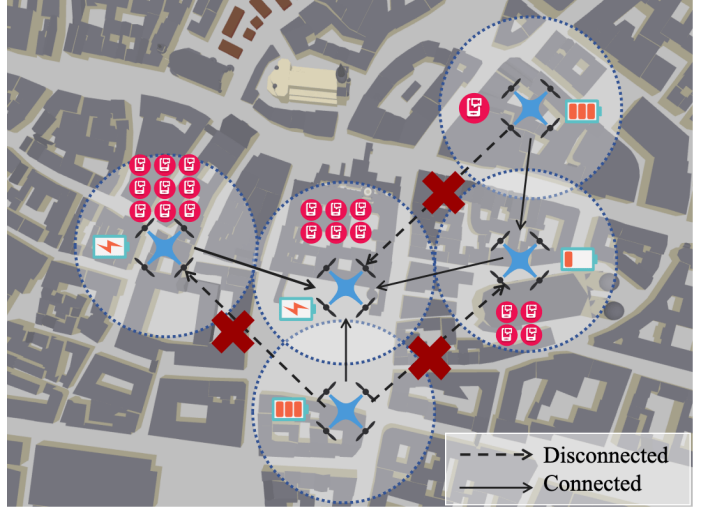


Fig. 1: A multi-UAV system serves ground UTs.

information across the multi-UAV network, complicating the development of a collaborative navigation strategy among all UAVs.

Recent studies have employed stacked graph layers to enhance UAV exploration in unobserved environments through message passing. This approach enables dynamic interaction between each UAV's actions and their neighboring UAVs' local observations in subsequent time slots [1]. As shown in Fig. 2, UAVs can aggregate observation information from multi-hop neighbors through stacked graph layers. These complex UAV-UT-environment interactions can be modeled as a Markov Decision Process (MDP) [5]. Based on the MDP formulation, existing work has extensively applied multi-agent reinforcement learning (MARL) to navigate and control a swarm of UAVs in dynamic and time-varying environments. However, simultaneously maximizing coverage and lifetime poses a significant challenge on traditional MARL frameworks. The pursuit of lifetime maximization often comes at the cost of reduced coverage efficiency. To handle dual objectives, existing studies typically combine both objectives into a weighted sum, where the weighting coefficient must be carefully tuned to balance the priorities of the two objectives. Determining an appropriate weighting coefficient is a time-consuming task that often requires heuristic and exhaustive search. The task becomes particularly challenging when the two objectives operate at different numerical scales, as proper coefficient calibration is crucial to prevent the larger-valued objective from disproportionately influencing the solutions,

The preliminary version of this article has been submitted to the 2025 IEEE Global Communications Conference for consideration.

Haoran Peng, and Ying-Jun Angela Zhang are with the Department of Information Engineering, The Chinese University of Hong Kong, Shatin, N.T., Hong Kong, P.R.China (Email: {hrpeng, yjzhang}@ie.cuhk.edu.hk).

Corresponding author: Ying-Jun Angela Zhang.

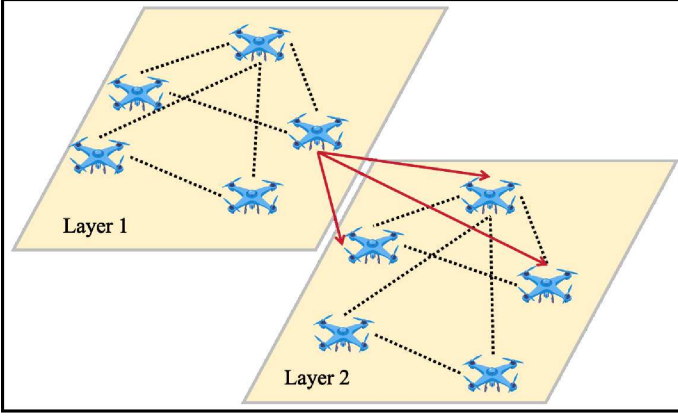


Fig. 2: The information aggregation through message passing.

regardless of its intended priority [6].

In contrast to conventional weighted-sum methods that struggle with scale disparities, we propose a Graph Attention-based Decentralized Actor-Critic (GADC) to separately optimize the prioritized dual objectives while aggregating information from neighboring UAVs (nodes) using a graph attention network (GAT) with multihead convolutional kernels. The architecture employs two specialized critic networks: a *coverage-effectiveness critic* for coverage optimization and a *lifetime-aware critic* for maximizing operational duration. The coverage-effectiveness critic primarily focuses on maximizing the coverage of UTs by the multi-UAV system, while the lifetime-aware critic serves as a secondary critic, aiming to extend the UAV system's battery life without compromising the coverage performance beyond a controllable threshold. The coverage-effectiveness critic and the lifetime-aware critic iteratively guide the training process of the dual-objective policy. Specifically, we impose a stringent constraint on the Kullback-Leibler (KL) divergence to restrict the adjustment of the lifetime-aware updating within a trust region bounded by the coverage-effectiveness strategy, using the probability ratio between these policies to enforce this constraint. GADC significantly enhances dual-objective optimization, as elucidated in [7]:

- Each objective is optimized via a specialized neural network and corresponding objective function, thereby facilitating rapid convergence.
- The maximization of UAVs' lifespan is judiciously constrained by a KL divergence factor linked to the primary objective, so that lifespan extension does not compromise the coverage performance beyond a controllable threshold. In contrast to the traditional approach that optimizes a weighted sum of both objectives, our approach prevents the larger-valued objective from dominating the solution space.

Contributions— This study investigates a multi-UAV system that prioritizes maximizing service coverage as the primary objective while also seeking to extend battery life. To address the decentralized nature of UAV operation, we propose an innovative GADC solution that leverages GAT layers to aggregate information from neighboring UAVs and

jointly optimize the prioritized dual objectives through two specialized critic networks. Our contributions are summarized as follows.

- *Multi-layer GAT for Enhanced Environmental Understanding:* We introduce a GADC that aggregates information from neighboring UAVs (nodes) and investigates unobserved areas using multiple GAT layers. This enables comprehensive environmental data assimilation beyond immediate observational coverage.
- *Separate Critic Networks for Efficient Dual-Objective Optimization:* The proposed GADC ensures rapid convergence of the dual-objective policy to the near-optimal solution of respective objectives within a defined trust region. The KL divergence factor, based on the probability ratio of the two strategies, effectively prevents the larger-valued objective from overshadowing the solution. We derive the performance upper and lower bounds of the proposed GADC framework.
- *Real-World Validation through Digital Twin:* We integrate ray tracing between UAVs and UTs to enhance the real-world applicability of the trained model. The GADC demonstrates superior performance in NVIDIA Sionna's Munich City digital twin environment, achieving 50% faster convergence and outperforming conventional approaches in both service coverage and system lifetime. Simulations show that GADC improves the convergence speed by 50% and outperforms the traditional algorithm in both service coverage and system lifetime.

The rest of the paper is structured as follows. Section II reviews the state-of-the-art literature. Section III presents the system model. The system operation and the proposed GADC are detailed in Section IV. Section V gives numerical results. Finally, Section VI concludes the paper.

II. RELATED WORKS

A. UAV-assisted Cellular Connectivity

Owing to their exceptional mobility, UAVs enable rapid connectivity in communication-challenged and ad hoc environments [8], [9]. By integrating mobile edge computing (MEC) devices, UAV systems can significantly expand service coverage while alleviating the demands placed on base stations (BSs) [10]. However, limited onboard energy constitutes a critical challenge in the design of UAV systems, directly affecting their operational lifespan. To address this issue, [11] introduced a UAV-aided system that jointly optimizes the energy harvesting strategy, UAV trajectory, and allocation of computing resources to minimize energy consumption while maximizing system throughput. Meanwhile, multi-UAV systems have emerged as essential solutions for complex tasks [12]. For instance, the system discussed in [13] employs multiple UAVs as aerial relays to enhance UT-satellite connectivity. Building on this, [14] improves and secures uplink transmissions between UTs and satellites while adhering to stringent constraints on transmission power. Despite these advances, a significant challenge remains in the design of cooperative navigation and control for multi-UAV systems,

as each UAV is confined to local observations and lacks a comprehensive understanding of the broader environment.

B. Multi-UAV Control and Navigation

Early studies focused on centralized control of multi-UAV systems. For example, [15] developed a centralized optimization algorithm for UAV swarm management in multi-task tracking, considering the constraints of limited budgets and safe flight distances. To enhance network security and performance, [16] established a wireless mesh network among UAVs using a graph traversal and pathfinding algorithm for efficient communication and cryptographic techniques for data protection. Additionally, [17] investigates RL in centralized control to balance service coverage and energy efficiency in multi-UAV systems. However, centralized control and navigation may be expensive in ad hoc scenarios due to the need for an infrastructure. Consequently, [18] and [19] employed MARL to facilitate multi-UAV navigation through individual UAV learning within local environments, while maintaining cooperative decision-making. Furthermore, [1] leveraged GAT layers to enhance MARL's ability to acquire global information from neighboring UAVs, improving navigation efficiency.

While MARL marks a significant advance in decentralized UAV operations by enabling real-time decision-making, its approach to dual-objective optimization relies heavily on heuristic methods and requires substantial expertise in managing objective trade-offs.

III. SYSTEM MODEL

Suppose that M UTs and N UAVs are randomly distributed in a space with dimensions $E \times E$ units. Each UAV and UT is equipped with a single antenna. The heights of UAVs' antennas and UTs' antennas are fixed. The locations of the UTs remain unchanged within an episode and vary from one episode to another. Suppose that UAVs function as flying BSs to serve the UTs and are navigated according to the locations of UTs. The system maintains two types of communications: UAV-UAV links for information exchange between neighboring UAVs and UAV-UT links for service provisioning. Table I summarizes the key notations used throughout this paper.

A. UAV Observation Range, Service Range, and Communication Range

Suppose that UAV-UT communications occur through a time-varying multipath channel characterized by Rayleigh fading and path loss. A UT is said to be observable by a UAV only if the received channel power exceeds a threshold σ_o , and is said to be within the service range of a UAV if the received channel power surpasses σ_s , where $\sigma_s \geq \sigma_o$. In an open area, the channel power thresholds of σ_s and σ_o translate to a maximum horizontal service coverage radius R_s and an observation coverage radius R_o , respectively, as illustrated in Fig. 3(a). Fig. 4 shows that R_s is given by

$$R_s = \sqrt{D_s^2 - H^2}, \quad (1)$$

TABLE I: Glossary of Notations

Symbol	Description
M	The number of UTs
N	The number of UAVs
D_s	The maximum communication distance
R_s	The maximum horizontal service coverage
H	The altitude of UAV hovering
T	The number of total time slots
$c_n(t)$	The number of UTs within the service coverage of the UAV n
$\omega_{m,n}^s(t)$	The service coverage indicator of the UT n and the UAV m
G_n	The undirected one-hop graph of the UAV n
L	The set of edges in graph G_n
$l_{n,i}$	The transmission link from the UAV-BS n to a neighboring UAV-BS i
\mathcal{A}	The adjacency matrix of graph G_n
\mathcal{V}	The set of nodes in graph G_n
Δt	The duration of a time slot
p_n^s	The transmit power for the link from UAV n to any UTs it serves
$\rho_{n,i}$	The energy consumed on transmission from UAV n to UAV i
χ_h	The hovering energy consumption for a UAV
$B_n(t)$	The residual energy of the UAV n at the end of time slot t
T_{net}	The network lifetime of the UAV-BS system
$\Gamma_{n,i}$	The transmission rate of $l_{n,i}$
$h_n(t)$	The hidden state for UAV n at the time slot t in the memory unit
g_n	The self-attention operation for UAV n

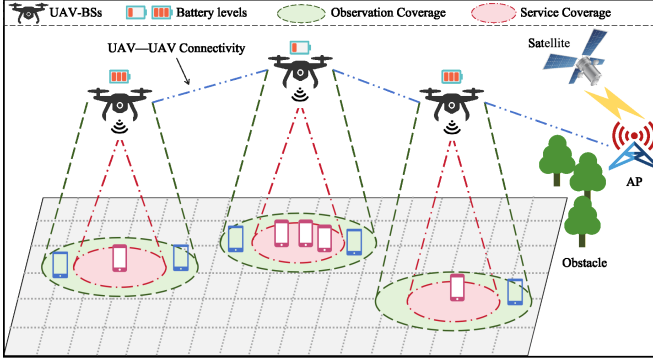
where D_s is the distance at which the received power equals σ_s , and H denotes the UAV operation height. Conversely, urban environments, obstacles like buildings and trees can block transmission links between a UT and UAVs, even when the UT is close to a UAV, as illustrated in Fig. 3(b). Consequently, a UT's observability or serviceability by a UAV depends solely on the received power level relative to thresholds σ_o and σ_s , rather than the geometric distance.

Suppose that each UT is served by one UAV only, even if it is within the service range of multiple UAVs. A UT becomes isolated if it is not within the service range of any UAVs. The selection of the serving UAV is influenced by the residual energy of the UAVs, the channel state of the propagation paths, the UAV's mobility cost, and other criteria detailed in Section IV. The number of UTs served by the n^{th} UAV during time slot t is:

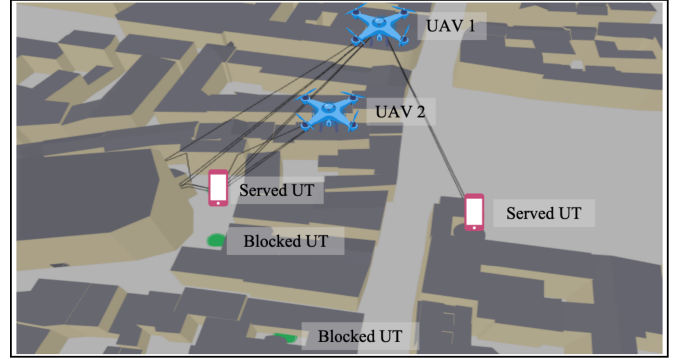
$$c_n(t) = \sum_{m=1}^M \omega_{m,n}^s(t), \quad (2)$$

where $\omega_{m,n}^s(t) = 1$ indicates that UT m is served by the n^{th} UAV during time slot t and $\omega_{m,n}^s(t) = 0$ otherwise. $\sum_{n=1}^N \omega_{m,n}^s(t) \leq 1, \forall m$ indicates that a UT is served by at most one UAV during a time slot.

For UAV-UAV communications, each UAV can establish



(a) The open area scenario.



(b) The urban scenario.

Fig. 3: The illustration of observation and service coverage of the multi-UAV system.

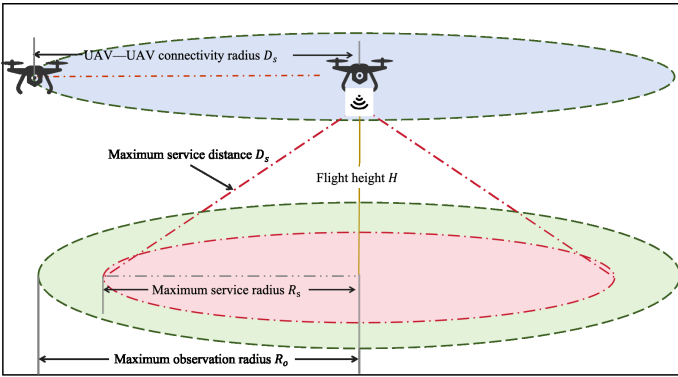


Fig. 4: The observation, service, and connectivity distance.

a direct line-of-sight (LoS) link with other UAVs within a connectivity distance threshold of D_s , as illustrated in Fig. 4. Define a connectivity matrix \mathcal{A} , where $\mathcal{A}(n, i) = 1$ when a direct connection exists between UAV i and UAV n ; and $\mathcal{A}(n, i) = 0$ otherwise.

B. The UAV energy consumption

A UAV's energy consumption consists of four components. First, navigation energy $\kappa\eta_n(t)$ is linearly proportional to the flight distance, where $\eta_n(t)$ represents UAV n 's horizontal movement during time slot t , and κ is a constant coefficient. Second, energy consumption for ground services during time slot t , given by $\Delta t c_n^s(t) p_n^s$, is proportional to the time slot duration Δt , the number of served UTs $c_n^s(t)$, and UAV n 's fixed transmit power p_n^s to the UTs. Third, suppose that each pair of neighboring UAVs (i.e., UAVs with direct communication connection) have one round of communication in each time slot to exchange their local observation data. Denote by $\rho_{n,i}(t)$ the inter-UAV communication energy thus consumed on transmission from UAV n to a neighboring UAV i ($i \neq n$). Last, a constant hovering energy χ_h for a UAV is consumed per time slot. The residual battery energy $b_n(t)$ of

the UAV n at the end of the t^{th} time slot is

$$b_n(t) = b_n(t-1) - \left(\chi_h + \sum_{i \in \mathcal{I}_n(t)} \rho_{n,i}(t) + \kappa\eta_n(t) + \Delta t c_n^s(t) p_n^s \right), \quad (3)$$

where $b_n(t-1)$ is the residual energy of UAV n at the end of the previous time slot. $\mathcal{I}_n(t)$ is the set of neighboring UAVs of UAV n at time t . We define this UAV network's lifetime as the time until the first UAV depletes its energy.

IV. GADC-BASED REINFORCEMENT LEARNING

A. Markov Decision Process for System Operation

Recall that we aim to enhance the UAV system's service coverage while maximizing the UAV network's lifetime. At the beginning of each time slot, UAVs make movement decisions based on their environmental observations. These actions influence their service range, observation range, and UAV-UAV connectivity, subsequently affecting service coverage and energy consumption. This decision-making process forms an MDP where current states and actions determine future outcomes. In this MDP, each UAV's state observation includes its current position, residual energy, the positions of the UTs within its service and observation ranges, and the locations of neighboring UAVs. The action space Γ for each UAV consists of 17 possible actions: movement in eight uniformly distributed directions, each with two distance options, plus one hovering (stationary) action. The action taken in time slot t influences other UAVs' observations (e.g., the set of neighboring UAVs, overlap of service regions, etc.) at the beginning of slot $t+1$. At each time step t , the system generates two instantaneous global rewards: an coverage-effectiveness reward $r^c(t) = \sum_{n=1}^N c_n(t)$ measuring service coverage and a lifetime-aware reward $r^f(t) = \min\{b_n(t)\}_{n=1}^N$ based on the residual battery energy to account for the lifetime of the UAV system. The corresponding long-term objectives for each UAV is

$$\mathcal{J} = \mathbb{E} \left[\sum_{t=0}^T \gamma^t r(t) \right], \quad (4)$$

where T represents the time horizon of UAV system operation. $\gamma \in [0, 1)$ is the discount factor weighing future rewards

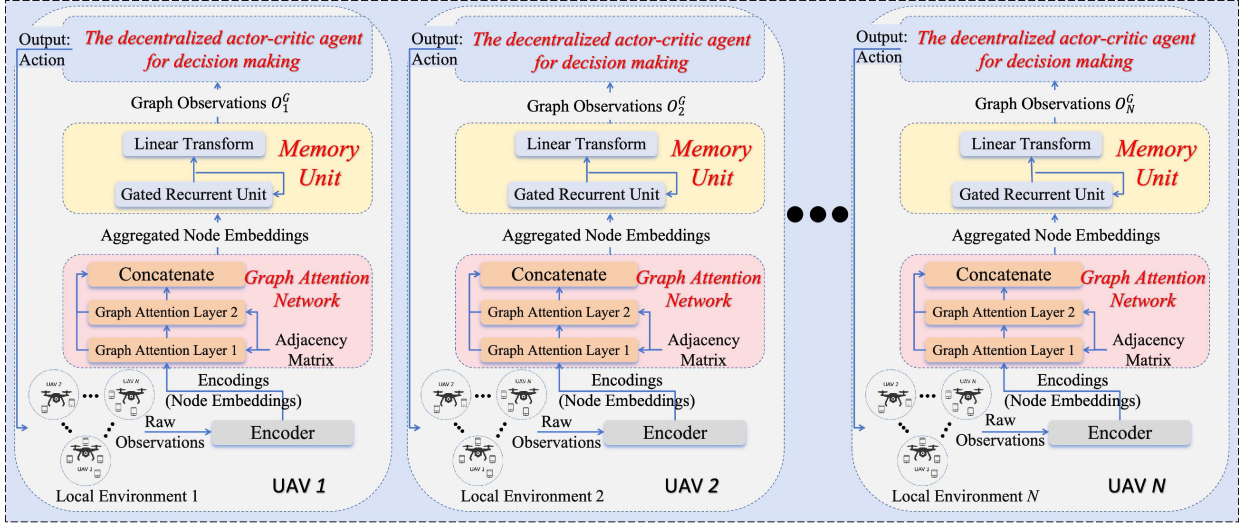


Fig. 5: The architecture of the proposed GADC-based RL.

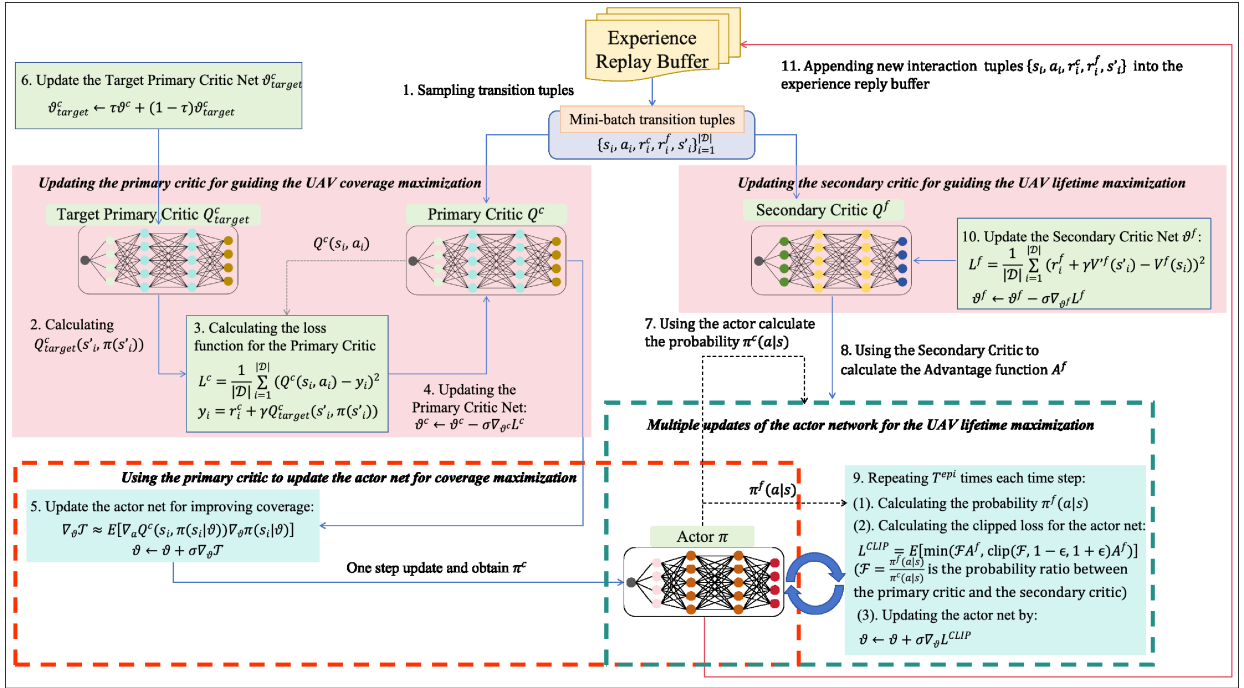


Fig. 6: The training processing of the proposed GADC-based decentralized actor-critic agent.

against immediate ones. The reward at time step t , denoted as $r(t)$, is influenced by two factors: the coverage-effectiveness reward $r^c(t)$ and the lifetime-aware reward $r^f(t)$. We iteratively refine the UAV's policy by incorporating the coverage-effectiveness and lifetime-aware objectives. In each iteration, we first maximize the UAVs' coverage through the coverage-effectiveness objective. Subsequently, we optimize the UAVs' operational lifetime within a constrained region surrounding the policy derived from the coverage-effectiveness objective.

B. System Architecture

Ideally, a global optimization of all UAVs' actions would optimize the coverage-effectiveness and lifetime-award rewards. In practice, however, each UAV makes decentralized

decisions based on its local observation. To bridge this gap between global optimality and local decision making, we propose a GADC-based RL framework. First, GADC employs a GAT that enables information exchange between neighboring UAVs, facilitating local-to-global knowledge propagation. Second, each UAV employs an actor-double-critic network to make autonomous decisions based on the information collected via the GAT, steering local decisions toward global optimization. As shown in Fig. 5, the proposed architecture processes raw UAV observations through a pipeline of four main stages. First, local observations of each UAV pass through an encoder to generate node embeddings. These embeddings then flow through a deep graph attention network comprising multiple GAT layers and a concentration layer, incorporating adjacency

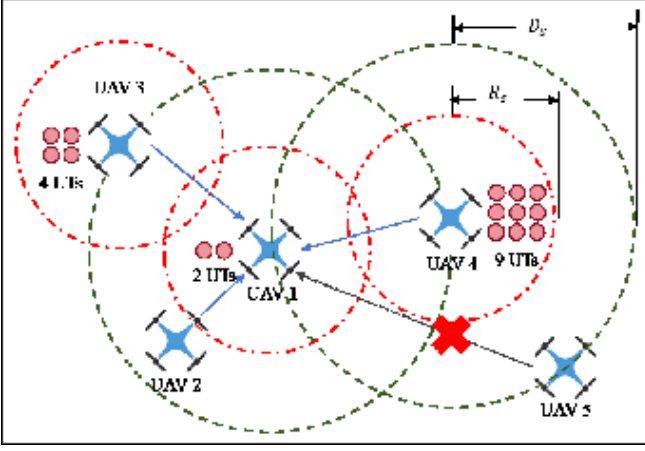


Fig. 7: The illustration of the message passing between UAVs.

matrix information. The aggregated node embeddings then enter a memory unit, where a Gated Recurrent Unit (GRU) followed by a linear transformation provides temporal context. Finally, these processed graph observations O_n^G serve as the input to an Actor-Critic network, where an Actor network determines actions while dual Critic networks (Coverage-effectiveness and Lifetime-aware) leverage an Experience Replay Buffer for action evaluation. Fig. 6 illustrates the training process of the Actor-Critic network, which will be discussed in the following sections.

C. Graph attention network for observation exploration

In this subsection, we detail the operation of the graph attention networks and memory units in Fig. 5. Consider an undirected graph $G(\mathcal{V}, L)$, where \mathcal{V} is the set of UAVs (nodes), L is the set of links (edges) connecting two neighboring UAVs, and \mathcal{A} is the adjacency matrix of G . Each UAV n 's local raw observation s_n includes its current position, residual energy, the positions of the UTs within its service and observation ranges, and the locations of neighboring UAVs. The local observation s_n is transformed to an embedding $\mu_n = ENC(s_n)$ through a common encoder function ENC .

In graph G , a UAV n 's attention to neighboring UAVs is weighted by their service loads, position, and residual energy. For example, as illustrated in Fig. 7, UAV 1 assigns a higher attention weight to UAV 4 (serving 9 UTs) compared to UAV 3 (serving 4 UTs). The GAT layer dynamically computes these attention weights, allowing each UAV to prioritize information from its neighbors based on their relative importance determined by service load, spatial relationship, and energy status. We formulate the self-attention in the GAT layers as

$$\alpha_{n,i} = \frac{\exp\left(\text{ReLU}\left((W_K \mu_i)^T \cdot W_Q \mu_n\right)\right)}{\sum_{l \in \mathcal{V}} \exp\left(\text{ReLU}\left((W_K \mu_l)^T \cdot W_Q \mu_n\right)\right)}, \quad (5)$$

where $\alpha_{n,i}$ is the attention weight that measures neighbor i 's importance to node n , computed using the self-attention mechanism's learnable matrices W_Q , W_K , and W_V for Query, Key, and Value operations, respectively. To address training instability from random initialization of matrices W_Q , W_K , and W_V , the architecture employs multihead attention with

J independent heads $\{\text{head}_1, \dots, \text{head}_J\}$. Each head j has its own learnable matrices W_Q^j , W_K^j , and W_V^j . Each node n aggregates the embedding of neighboring nodes as

$$g_n = \text{Concat}_{j=1}^J \left(\sum_{i \in I_n} \alpha_{n,i}^j \cdot W_V^j \mu_i \right). \quad (6)$$

While stacking more GAT layers would aggregate information from more neighboring nodes and enhance embedding information, it also increases computational overhead. To strike a balance, we employ a two-hop GAT architecture, allowing each node to gather embedding information from its first-hop and second-hop neighbors. As shown in Fig. 5, the aggregated embeddings from the encoder and GAT layers are concatenated to produce the final output, which is then fed into the memory unit.

In the memory unit, a GRU is implemented to store aggregated node embeddings from the last time slot to maintain temporal information. The GRU memory unit processes long-term memory according to

$$h_n(t) = \text{GRU}(g_n(t) \mid h_n(t-1)), \quad (7)$$

where $g_n(t)$ represents node n 's aggregated GAT embedding at time slot t , and $h_n(t-1)$ is node n 's hidden state from the previous time slot $t-1$. As shown in Fig. 5, the memory unit concludes with a linear transform that processes the hidden state $h_n(t) \mid_{t=T}$. Each UAV n 's final output denoted as $O_n^G(t)$, is the input to its actor-double-critic network.

D. The Actor-Critic networks

This subsection details the Actor-Critic networks module in Fig. 6. In the Actor-Critic networks, each agent's environment state is $s(t) = O_n^G(t)$, the output of the memory unit. The agent's actions influence the raw observations, which subsequently feed into the GAT. We define π^c and π^f as the coverage-effectiveness and lifetime-aware operations, respectively, for actor updates. The actor network's policy π is a combination of these two operations. The π^c represents the actor's policy after the coverage-effectiveness critic updates the actor network, while π^f denotes the policy after the lifetime-aware critic updates the actor network. As illustrated in Algorithm 1 and Fig. 6, the coverage-effectiveness critic and the lifetime-aware critic alternately optimize the actor network, managing the trade-off between the dual objectives. The notation $\mathcal{J}_{\pi^f}^c$ denotes the coverage-effectiveness objective when the actor network is trained by a combination of the coverage-effectiveness critic and lifetime-aware critic, while $\mathcal{J}_{\pi^c}^c$ denotes the pure coverage-effectiveness objective when the actor network is trained based on the coverage-effectiveness critic only. The discounted total return of $\mathcal{J}_{\pi^f}^c$ and $\mathcal{J}_{\pi^c}^c$ is defined by

$$\mathcal{J}_{\pi^f}^c = \mathbb{E}_{\substack{s \sim d^{\pi^f} \\ a \sim \pi^f}} \left[\sum_{t=0}^{\infty} \gamma^t r^c(s \mid a) \right] \quad (8)$$

and

$$\mathcal{J}_{\pi^c}^c = \mathbb{E}_{\substack{s \sim d^{\pi^c} \\ a \sim \pi^c}} \left[\sum_{t=0}^{\infty} \gamma^t r^c(s \mid a) \right], \quad (9)$$

Algorithm 1: The training process of the proposed GADC

```

1 Input:
2   The number of UAVs,  $N$ , and the number of UTs,  $M$ ;
3   The number of time slot  $T$  in each episode;
4 Initial: The actor network  $\pi$ , the primary critic network  $Q^c$ , the target primary critic network  $Q_{target}^c$ , and the
   secondary critic network  $Q^f$  for each agent  $n$ ;
5 Output: The optimal actor network for each agent  $n$ .
6 for each episode do
7   Randomly generate the position of UTs and UAVs in the given  $E \times E$  area;
8   for time step from  $t = 0$  to  $T$  do
9      $t = t + 1$ ;
10    for agent  $n = 1$  to  $N$  do
11      Obtain the raw observation  $s_n(t)$ , including its current position, residual energy, the positions of the UTs
        within its service and observation ranges, and the locations of neighboring UAVs;
12      Execute encoder function  $\mu_n = ENC(s_n)$  to generate the node embedding  $\mu_n$ ;
13      Use Eq. (5) to aggregate the node embeddings and extract the importance of neighboring UAVs;
14      Concatenate the node embeddings  $\mu_n$  and the output of GAT layers,  $g_n$ , as the input of the memory unit,
        GRU;
15      Obtain the state  $O_n^G(t)$  by concatenating the aggregated GAT embedding  $g_n(t)$  from the current time step
        with the hidden state  $h_n(t-1)$  of the GRU from the previous time step;
16      Select a action  $a_n(t)$  from the actor net using the input  $O_n^G(t)$ ;
17      Execute the action  $a_n(t)$  then obtain the coverage-effectiveness reward  $r_n^c(t)$ , the lifetime-award reward
         $r_n^f(t)$ , and the next raw state  $s_n(t+1)$ ;
18      Store the transition tuples  $\{s_n(t), a_n(t), r_n^c(t), r_n^f(t), s_n(t+1)\}$  into the replay buffer;
19      if Training==True then
20        Sample transition tuples  $\mathcal{D}$  from the replay buffer;
21        Update the primary critic by minimizing Eq. (12);
22        Optimize the coverage-effectiveness objective for the actor net by Eq. (14);
23        Use Eq. (15) to softly update the target primary critic network;
24        Use the sampled tuples and the updated actor to calculate the probability  $\pi^c(a | s)$ ;
25        for inner loop from 0 to  $T^{epi}$  do
26          Calculate the probability  $\pi^f(a | s)$  from the actor net;
27          Use Eq. (16) to calculate the clipped loss for the actor net;
28          Update the actor net by minimizing (16);
29        end
30        Update the lifetime-aware critic by minimizing Eq. (18);
31      end
32    end
33  end
34 end

```

respectively. In policy gradient methods, the advantage function is used to measure how much better (or worse) taking action a in state s is compared to the average action under policy π . Define the advantage function as

$$A^*(s, a) = Q^*(s, a) - V^*(s), \quad (10)$$

where $Q^*(s, a)$ denotes the action-value function and $V^*(s)$ represents the state-value function. The superscript $*$ can be substituted with c and f to indicate the coverage-effectiveness and lifetime-aware policies, respectively.

We implement a DDPG architecture where the coverage-effectiveness critic serves as the primary critic for maximizing the covered UTs among the multi-UAV system. The primary critic updates via temporal-difference (TD) error, using stochastic gradient descent to minimize the mean-squared error

(MSE) between its predictions and the target values from the lifetime-aware critic. In particular, the target of the TD error for any UAV n

$$y = r^c + \gamma Q_{target}^c(s', \pi(s')), \quad (11)$$

where π represents the combined policy of the UAV, and Q_{target}^c is the target critic network used to update the primary critic network, as is standard in DDPG architecture. For notation simplicity, we use s and s' to represent the environment states of the current and next time slots, respectively. The MSE for updating the primary critic is defined as

$$L^c = \frac{1}{|\mathcal{D}|} \sum_{i=1}^{|\mathcal{D}|} (Q^c(s_i, a_i) - y_i)^2, \quad (12)$$

$$\vartheta^c \leftarrow \vartheta^c - \sigma \nabla_{\vartheta^c} L^c,$$

where $\{(s_i, a_i, r_i^c, s'_i)\}_{i=1}^{|\mathcal{D}|}$ is the random mini-batch sampled from the replay buffer, and σ is the learning rate.

Subsequently, we employ the updated primary critic network of Eq. (12) to enhance the coverage-effectiveness policy of the actor network. To improve the coverage performance, the actor network is refined by maximizing the expected return derived from the output of the primary critic network, denoted as Q^c . The loss function for the actor network is defined as:

$$L(\vartheta) = -\frac{1}{|\mathcal{D}|} \sum_{i=1}^{|\mathcal{D}|} [Q^c(s_i, \pi(s_i | \vartheta))], \quad (13)$$

where ϑ is the parameters of the actor network, $Q^c(s_i, \pi(s_i | \vartheta))$ denotes the estimated value of taking the action produced by the actor network $\pi(s_i | \vartheta)$ and the state s_i , evaluated by the primary critic network Q^c . We then update the actor network's parameters using the following use the chain rule:

$$\begin{aligned} \nabla_{\vartheta} \mathcal{J}^c &\approx \mathbb{E}_s [\nabla_a Q^c(s, a) |_{a \sim \pi(s)} \nabla_{\vartheta} \pi(s)], \\ \vartheta &\leftarrow \vartheta + \sigma \nabla_{\vartheta} \mathcal{J}^c. \end{aligned} \quad (14)$$

The target primary critic network is updated softly using the following method:

$$\vartheta_{target}^c \leftarrow \tau \vartheta^c + (1 - \tau) \vartheta_{target}^c \quad (15)$$

where ϑ_{target}^c and ϑ^c are the parameters in the target primary critic network and the primary critic network, respectively. $\tau \in (0, 1)$ is a small positive constant, controlling the update rate.

Likewise, the secondary (lifetime-aware) critic network is trained to maximize the minimum residual energy across all UAVs. However, since this lifetime-aware objective may compromise coverage-effectiveness optimization, each agent's lifetime-aware optimization needs to be constrained within an acceptable effectiveness loss threshold. To address this, we propose a proximal policy optimization (PPO)-based algorithm to update the secondary critic network while maintaining bounded effectiveness loss. Denote the *probability ratio* between the lifetime-aware policy, π^f , and the coverage-effectiveness policy, π^c , by $\mathcal{F} = \frac{\pi^f(a|s)}{\pi^c(a|s)}$. Typically, the primary critic updates the actor once per time step, while the secondary critic updates the actor T^{epi} times during each time step. The notation $\pi^c(a | s)$ represents the probability of the actor selecting action a given state s after the actor policy π^c is updated by the primary critic. In contrast, $\pi^f(a | s)$ denotes the probability derived after the actor policy is updated by the secondary critic during each iteration of the T^{epi} -times for-loop optimization. The actor network is updated by minimizing the clipped objective function, which can be given by

$$\begin{aligned} L^{CLIP}(\vartheta) &= \mathbb{E} [\min(\mathcal{F} A^f, \text{clip}(\mathcal{F}, 1 - \epsilon, 1 + \epsilon) A^f)], \\ \vartheta &\leftarrow \vartheta + \sigma \nabla_{\vartheta} L^{CLIP}(\vartheta), \end{aligned} \quad (16)$$

where $\epsilon \in [0.1, 0.4]$ is a hyperparameter, and A^f is the estimated advantage of the lifetime-aware objective. The secondary critic's advantage function A^f for each agent n can be denoted by

$$A^f = r^f + \gamma V'^f(s') - V^f(s), \quad (17)$$

where $V'^f(s')$ is the state-value function of the lifetime-aware policy of the agent n for the next time step $t + 1$. Furthermore, the secondary critic is updated by minimizing the following loss function

$$\begin{aligned} L^f &= \frac{1}{|\mathcal{D}|} \sum_{i=1}^{|\mathcal{D}|} \left(r^f + \gamma V'^f(s') - V^f(s) \right)^2, \\ \vartheta^f &\leftarrow \vartheta^f - \sigma \nabla_{\vartheta^f} L^f, \end{aligned} \quad (18)$$

where ϑ^f is the parameter of the secondary critic network.

Before proving the performance bound of the proposed GADC, we briefly introduce the foundational lemma of the Performance Difference Lemma. This lemma states that the difference in expected performance between two policies can be expressed in terms of the advantage function and the action probabilities of the policies [20]. In policy gradient methods, the lemma allows for deriving the policy gradient update rule. The expected improvement can be calculated using the advantage estimates, guiding the optimization of the policy. Formally, if you have two policies π and π' , the lemma can be stated as:

$$V^{\pi'}(s) - V^{\pi}(s) = \mathbb{E}_{a \sim \pi'} [A^{\pi}(s, a)] \quad (19)$$

where $V^{\pi}(s)$ is the expected return when following policy π from state s , $A^{\pi}(s, a)$ is the advantage function, which measures the action a in state s is compared to the average action under policy π .

In each time step, $\mathcal{J}_{\pi^f}^c$ represents the objective of the actor's policy guided by both the coverage-effectiveness critic and the lifetime-aware critic. In contrast, $\mathcal{J}_{\pi^c}^c$ denotes the objective of the actor's policy when guided solely by the coverage-effectiveness critic, prior to any updates from the lifetime-aware critic. We present the performance difference bound lemma between $\mathcal{J}_{\pi^c}^c$ and $\mathcal{J}_{\pi^f}^c$ as follows:

Lemma 1. *Given two policies π^f and π^c , the performance difference between $\mathcal{J}_{\pi^c}^c$ and $\mathcal{J}_{\pi^f}^c$ is bounded by*

$$\mathcal{J}_{\pi^f}^c - \mathcal{J}_{\pi^c}^c \leq \frac{1}{1 - \gamma} \mathbb{E}_{\substack{s \sim d^{\pi^c} \\ a \sim \pi^f}} [A^c(s, a)] + \frac{\sqrt{2\delta} \gamma \epsilon^{\pi^f}}{(1 - \gamma)^2}, \quad (20)$$

and

$$\mathcal{J}_{\pi^f}^c - \mathcal{J}_{\pi^c}^c \geq \frac{1}{1 - \gamma} \mathbb{E}_{\substack{s \sim d^{\pi^c} \\ a \sim \pi^f}} [A^c(s, a)] - \frac{\sqrt{2\delta} \gamma \epsilon^{\pi^f}}{(1 - \gamma)^2}, \quad (21)$$

where δ denotes the specified constraint region for the Kullback-Leibler (KL) divergence between the two policies. The maximum expected value of the advantage function across all states is $\epsilon^{\pi^f} = \max_s |\mathbb{E}_{a \sim \pi^f} [A^c(s, a)]|$.

Proof. First note that $A^c(s, a) = r^c(s, a) + \gamma V^{\pi^c}(s') - V^{\pi^c}(s)$. We start with the Performance Difference Lemma [20], which states that the discounted total effectiveness return for the

combination of π^f and π^c is:

$$\begin{aligned}
\mathcal{J}_{\pi^f}^c &= \mathbb{E}_{\substack{s \sim d^{\pi^f} \\ a \sim \pi^f}} \left[\sum_{t=0}^{\infty} \gamma^t r^c(s | a) \right] \\
&= \mathbb{E}_{\substack{s \sim d^{\pi^f} \\ a \sim \pi^f}} \left[\sum_{t=0}^{\infty} \gamma^t r^c(s, a) - \sum_{t=0}^{\infty} \gamma^t V^{\pi^c}(s) + \sum_{t=0}^{\infty} \gamma^t V^{\pi^c}(s) \right] \\
&= \mathbb{E}_{\substack{s \sim d^{\pi^f} \\ a \sim \pi^f}} \left[\sum_{t=0}^{\infty} \gamma^t r^c(s, a) - \sum_{t=0}^{\infty} \gamma^t V^{\pi^c}(s) + \sum_{t=0}^{\infty} \gamma^{t+1} V^{\pi^c}(s') \right] \\
&\quad + \mathbb{E}_{s_0 \sim d^{\pi^c}} [V^{\pi^c}(s_0)] \\
&= \mathbb{E}_{\substack{s \sim d^{\pi^f} \\ a \sim \pi^f}} \left[\sum_{t=0}^{\infty} \gamma^t (r^c(s, a) + \gamma V^{\pi^c}(s') - V^{\pi^c}(s)) \right] \\
&\quad + \mathbb{E}_{s_0 \sim d^{\pi^c}} [V^{\pi^c}(s_0)] \\
&= \mathbb{E}_{\substack{s \sim d^{\pi^f} \\ a \sim \pi^f}} \left[\sum_{t=0}^{\infty} \gamma^t (Q^{\pi^c}(s, a) - V^{\pi^c}(s)) \right] + \mathbb{E}_{s_0 \sim d^{\pi^c}} [V^{\pi^c}(s_0)] \\
&= \mathbb{E}_{\substack{s \sim d^{\pi^f} \\ a \sim \pi^f}} \left[\sum_{t=0}^{\infty} \gamma^t A^c(s, a) \right] + \mathcal{J}_{\pi^c}^c \\
&= \frac{1}{1-\gamma} \mathbb{E}_{\substack{s \sim d^{\pi^f} \\ a \sim \pi^f}} [A^c(s, a)] + \mathcal{J}_{\pi^c}^c.
\end{aligned} \tag{22}$$

So we have

$$\mathcal{J}_{\pi^f}^c - \mathcal{J}_{\pi^c}^c = \frac{1}{1-\gamma} \mathbb{E}_{\substack{s \sim d^{\pi^f} \\ a \sim \pi^f}} [A^c(s, a)]. \tag{23}$$

Therefore,

$$\mathcal{J}_{\pi^f}^c - \mathcal{J}_{\pi^c}^c = \frac{1}{1-\gamma} \left(\mathbb{E}_{\substack{s \sim d^{\pi^f} \\ a \sim \pi^f}} [A^c(s, a)] - \mathbb{E}_{\substack{s \sim d^{\pi^c} \\ a \sim \pi^c}} [A^c(s, a)] \right). \tag{24}$$

The term $\mathbb{E}_{\substack{s \sim d^{\pi^f} \\ a \sim \pi^f}} [A^c(s, a)]$ represents the inner product of d^{π^c} and $\mathbb{E}_{a \sim \pi^f} [A^c(s, a)]$:

$$\begin{aligned}
\mathbb{E}_{\substack{s \sim d^{\pi^f} \\ a \sim \pi^f}} [A^c(s, a)] &= \left\langle d^{\pi^f}, \mathbb{E}_{a \sim \pi^f} [A^c(s, a)] \right\rangle \\
&= \left\langle d^{\pi^c}, \mathbb{E}_{a \sim \pi^f} [A^c(s, a)] \right\rangle + \left\langle d^{\pi^f} - d^{\pi^c}, \mathbb{E}_{a \sim \pi^f} [A^c(s, a)] \right\rangle \\
&= \mathbb{E}_{\substack{s \sim d^{\pi^c} \\ a \sim \pi^f}} [A^c(s, a)] + \left\langle d^{\pi^f} - d^{\pi^c}, \mathbb{E}_{a \sim \pi^f} [A^c(s, a)] \right\rangle.
\end{aligned} \tag{25}$$

By applying Holder's inequality, the last term in Eq. (25) is bounded by

$$\begin{aligned}
&\left| \left\langle d^{\pi^f} - d^{\pi^c}, \mathbb{E}_{a \sim \pi^f} [A^c(s, a)] \right\rangle \right| \\
&\leq \|d^{\pi^f} - d^{\pi^c}\|_p \left\| \mathbb{E}_{a \sim \pi^f} [A^c(s, a)] \right\|_q,
\end{aligned} \tag{26}$$

where $p, q \in [1, +\infty]$ satisfy $\frac{1}{p} + \frac{1}{q} = 1$. Combining Eqs. (25)

and (26), we have the following bound

$$\begin{aligned}
&\mathbb{E}_{\substack{s \sim d^{\pi^f} \\ a \sim \pi^f}} [A^c(s, a)] \leq \\
&\mathbb{E}_{\substack{s \sim d^{\pi^c} \\ a \sim \pi^f}} [A^c(s, a)] + \|d^{\pi^f} - d^{\pi^c}\|_p \left\| \mathbb{E}_{a \sim \pi^f} [A^c(s, a)] \right\|_q,
\end{aligned} \tag{27}$$

and

$$\begin{aligned}
&\mathbb{E}_{\substack{s \sim d^{\pi^f} \\ a \sim \pi^f}} [A^c(s, a)] \geq \\
&\mathbb{E}_{\substack{s \sim d^{\pi^c} \\ a \sim \pi^f}} [A^c(s, a)] - \|d^{\pi^f} - d^{\pi^c}\|_p \left\| \mathbb{E}_{a \sim \pi^f} [A^c(s, a)] \right\|_q.
\end{aligned} \tag{28}$$

We choose $p = 1$ and $q = \infty$. The total variation (TV) distance between the discounted future state distributions d^{π^c} and d^{π^f} is expressed using the L1-norm as follows:

$$\|d^{\pi^f} - d^{\pi^c}\|_1 = 2D_{TV}(d^{\pi^f} \| d^{\pi^c}). \tag{29}$$

The infinite norm of the expected value of the advantage function $\mathbb{E}_{a \sim \pi^f} [A^c(s, a)]$ is denoted as

$$\left\| \mathbb{E}_{a \sim \pi^f} [A^c(s, a)] \right\|_{\infty} = \max_s \left| \mathbb{E}_{a \sim \pi^f} [A^c(s, a)] \right|. \tag{30}$$

We let $\epsilon^{\pi^f} = \max_s |\mathbb{E}_{a \sim \pi^f} [A^c(s, a)]|$ for notation simplicity. By combining Eqs. (22), (27) and (28), we have the following bounds

$$\begin{aligned}
&\mathcal{J}_{\pi^f}^c - \mathcal{J}_{\pi^c}^c \\
&\leq \frac{1}{1-\gamma} \left(\mathbb{E}_{\substack{s \sim d^{\pi^c} \\ a \sim \pi^f}} [A^c(s, a)] + 2D_{TV}(d^{\pi^f} \| d^{\pi^c}) \epsilon^{\pi^f} \right),
\end{aligned} \tag{31}$$

and

$$\begin{aligned}
&\mathcal{J}_{\pi^f}^c - \mathcal{J}_{\pi^c}^c \\
&\geq \frac{1}{1-\gamma} \left(\mathbb{E}_{\substack{s \sim d^{\pi^c} \\ a \sim \pi^f}} [A^c(s, a)] - 2D_{TV}(d^{\pi^f} \| d^{\pi^c}) \epsilon^{\pi^f} \right).
\end{aligned} \tag{32}$$

The TV distance of the discounted future state distribution under π^c and π^f is bounded by

$$D_{TV}(d^{\pi^f} \| d^{\pi^c}) \leq \frac{\gamma}{1-\gamma} \mathbb{E}_{s \sim d^{\pi^c}} [D_{TV}(\pi^f \| \pi^c)[s]], \tag{33}$$

where $D_{TV}(\pi^f \| \pi^c)[s] = (1/2) \sum_a |\pi^f(a | s) - \pi^c(a | s)|$. Therefore, the bounds of Eqs. (31) and (32) can be rewritten as

$$\begin{aligned}
&\mathcal{J}_{\pi^f}^c - \mathcal{J}_{\pi^c}^c \leq \\
&\frac{1}{1-\gamma} \left(\mathbb{E}_{\substack{s \sim d^{\pi^c} \\ a \sim \pi^f}} [A^c(s, a)] + \frac{2\gamma}{1-\gamma} \mathcal{E}_{TV}(\pi^f \| \pi^c) \epsilon^{\pi^f} \right),
\end{aligned} \tag{34}$$

and

$$\begin{aligned}
&\mathcal{J}_{\pi^f}^c - \mathcal{J}_{\pi^c}^c \geq \\
&\frac{1}{1-\gamma} \left(\mathbb{E}_{\substack{s \sim d^{\pi^c} \\ a \sim \pi^f}} [A^c(s, a)] - \frac{2\gamma}{1-\gamma} \mathcal{E}_{TV}(\pi^f \| \pi^c) \epsilon^{\pi^f} \right),
\end{aligned} \tag{35}$$

respectively, where

$$\mathcal{E}_{TV}(\pi^f \parallel \pi^c) = \mathbb{E}_{s \sim d^{\pi^c}} \left[D_{TV}(\pi^f \parallel \pi^c) [s] \right]. \quad (36)$$

By applying Pinsker's inequality, the expected value of the TV distance under π^c and π^c is bounded by

$$\mathbb{E}_{s \sim d^{\pi^c}} \left[D_{TV}(\pi^f \parallel \pi^c) [s] \right] \leq \mathbb{E}_{s \sim d^{\pi^c}} \left[\sqrt{\frac{1}{2} D_{KL}(\pi^f \parallel \pi^c) [s]} \right], \quad (37)$$

where $D_{KL}(\pi^f \parallel \pi^c)$ is the KL divergence between π^f and π^c . The KL divergence factor constrains the variation of the UAV policy within a specified region of the effectiveness objective while optimizing the UAV policy using the lifetime-aware objective at each iteration. This constraint ensures that the maximum divergence of the probability distribution between π^f and π^c is less than δ :

$$\max_{s \sim d^{\pi^c}} \mathbb{E} \left[D_{KL}(\pi^f \parallel \pi^c) \right] \leq \delta. \quad (38)$$

Therefore, bounds (34) and (35) can be derived as

$$\mathcal{J}_{\pi^f}^c - \mathcal{J}_{\pi^c}^c \leq \frac{1}{1-\gamma} \mathbb{E}_{\substack{s \sim d^{\pi^c} \\ a \sim \pi^f}} [A^c(s, a)] + \frac{\sqrt{2\delta}\gamma\epsilon^{\pi^f}}{(1-\gamma)^2}, \quad (39)$$

and

$$\mathcal{J}_{\pi^f}^c - \mathcal{J}_{\pi^c}^c \geq \frac{1}{1-\gamma} \mathbb{E}_{\substack{s \sim d^{\pi^c} \\ a \sim \pi^f}} [A^c(s, a)] - \frac{\sqrt{2\delta}\gamma\epsilon^{\pi^f}}{(1-\gamma)^2}, \quad (40)$$

respectively. \square

V. PERFORMANCE EVALUATION

We conduct a comparative analysis of the proposed GADC-based RL and state-of-the-art approaches, including the traditional multi-agent DDPG (MADDPG), GAT-based MADDPG, and exhaustive search (ES). Notably, the GAT-based MADDPG algorithm utilizes the same GAT architecture and memory units as the proposed GADC. Specifically, the reward structures for ES, MADDPG, and GAT-based MADDPG are formulated as:

$$\hat{r} = \varphi r^c + (1 - \varphi) r^f, \quad (41)$$

where $\varphi \in (0, 1)$ denotes the coefficient that balances the two objectives. Given that, the action space grows exponentially as $|\mathcal{U}|^N$, where $|\mathcal{U}|$ is the individual action space size, ES becomes computationally impractical. To address this limitation, we implement 10^7 random action selections at each time step, selecting the one that yields the highest reward as the ES reward. The hardware specifications and software versions used in our simulations are detailed in Table II, with the simulation parameters provided in Table III.

A. Performance evaluation in the Python/Matlab simulator

The simulation environment uses a 200×200 unit map with a communication radius $R_s = 10$ units. The neural network architecture employs hidden layers of 256 neurons each, and the attention mechanism uses four heads per kernel. In the training phase, we configure the system with 20 UAVs and

TABLE II: Software & hardware specifications

Device/Software	Specifications
CPU	Intel® Xeon® w9-3475X 2.20 GHz
RAM	256 GB
GPU	NVIDIA RTX A6000 (48GB)
Storage	SSD 2.0 TB / SATA 16.5 TB
OS	Ubuntu 22.04.2
Python	3.10.14
Pytorch	2.3.1
Tensorflow	2.15.1
Sionna	0.18.0

TABLE III: Simulation parameters in Sionna

Parameters	Value
The height of UT antenna	1.5 m
The height of UAV antenna	100 m
FFT size	64
Number of attention head	4
Raytracer sampling	Fibonacci sphere
Max depth of rays	2
Launch rays	10^6
Normalize delays	True
Synthetic antenna array	True

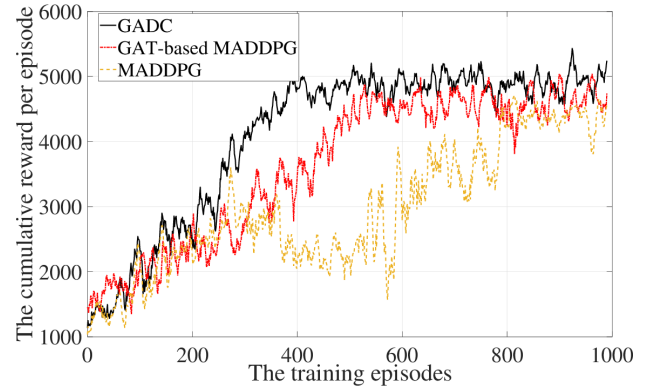
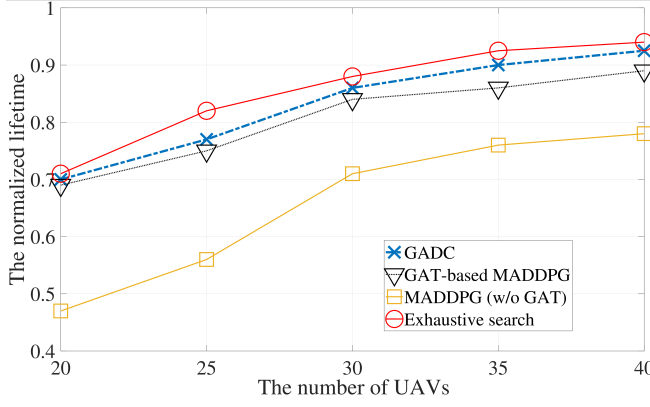


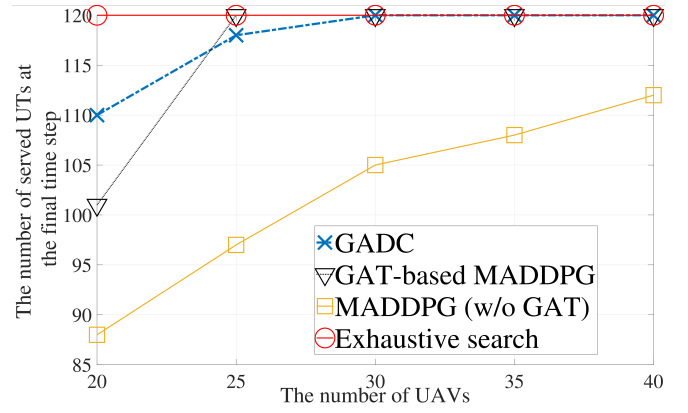
Fig. 8: The convergence performance of different algorithms in the ideal setting.

120 UTs. Unless otherwise stated, the number of UTs remains at 120 for testing, while the number of UAVs varies between 20 to 40.

Fig. 8 compares the convergence performance of different algorithms. Notably, GADC achieves convergence at 500 episodes, while the GAT-based MADDPG and MADDPG require more than 700 episodes to converge. While the benchmark algorithms eventually converge to similar reward levels due to careful selection of coefficient φ for UAV lifetime performance, the proposed GADC-based approach exhibits faster convergence without the need of careful selection of the weighting coefficient. Moreover, the proposed GADC shows fluctuations around episode 800, likely due to continued exploration post-convergence as the learning agents (UAVs) balance exploration and exploitation. The superior performance of GADC over conventional MADDPG in both convergence

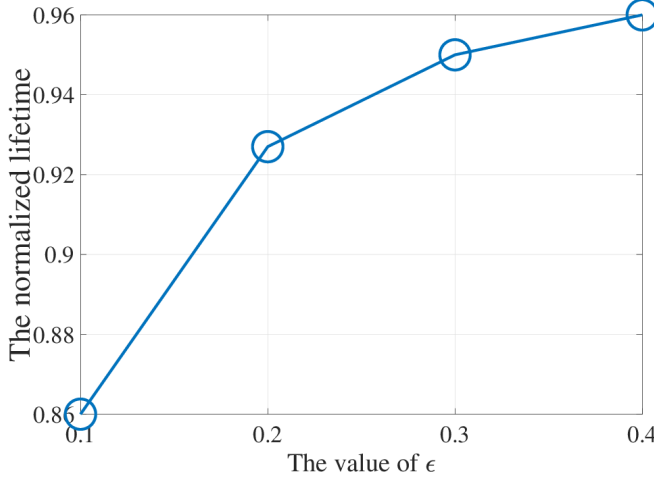
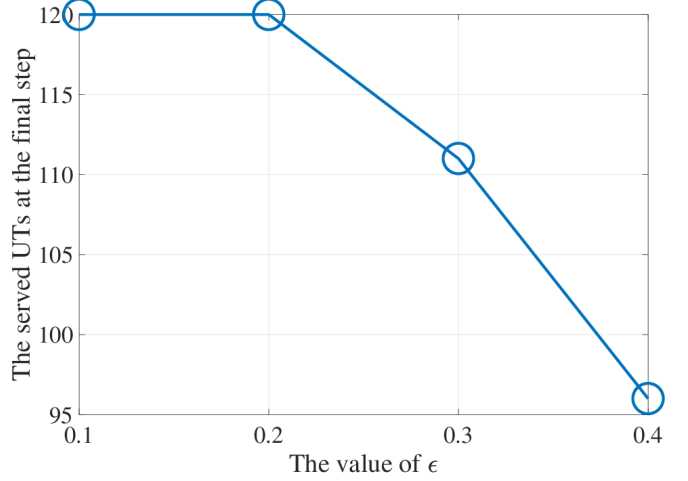


(a) The impact on the lifetime performance.



(b) The impact on the effective coverage performance.

Fig. 9: The impact of the number of UAVs on different objectives.

(a) The impact of ϵ on the lifetime-aware objective.(b) The impact of ϵ on the effectiveness objective.Fig. 10: The impact of ϵ on the proposed GADC.

speed and cumulative reward can be attributed to the GAT and memory units enriching the UAVs' information.

Fig. 9(a) illustrates the UAV lifetime of the proposed GADC alongside benchmark algorithms as the number of UAVs increases from 20 to 40. The figure reveals that the proposed GADC and GAT-based MADDPG significantly outperforms the conventional MADDPG, approaching the optimal solution achieved by ES. The superior performance stems from the GAT architecture's ability to aggregate information from indirectly connected UAVs, whereas conventional MADDPG struggles with partial observations. As the number of UAV-BSs increases, all algorithms show improved lifetime because higher UAV counts reduce the average service load per UAV, resulting in decreased movement frequency. The reduced movement requirements naturally lead to extended UAV operational lifetimes.

Fig. 9(b) compares the service coverage between GADC and the benchmark algorithms. Since each UT position remains fixed throughout the episodes, UAVs tend to stabilize their positions to minimize energy consumption once they reach their policy-determined optimal deployment. The figure demonstrates that the ES approach achieves complete UT coverage across all scenarios from 20 to 40 UAVs. Remarkably,

the proposed GADC and GAT-based MADDPG algorithms ensure coverage for all UTs when the number of UAVs exceeds 30. In contrast, the conventional MADDPG fails to provide favorable service coverage, even with 40 UAVs.

Figs. 10(a) and 10(b) illustrate the impact of the parameter ϵ on the lifetime-aware and effectiveness objectives, respectively. It is evident that an increase in ϵ correlates with enhanced lifetime performance, at the expense of the number of served UTs in the service area. This phenomenon occurs because a smaller ϵ tightly constrains the lifetime-aware policy to the effectiveness policy, resulting in conservative updates that closely follow the effectiveness objective. In contrast, a larger ϵ permits greater divergence between the effectiveness and lifetime-aware policies, allowing more aggressive updates in the lifetime-aware policy that can significantly deviate from the effectiveness goal. Since the effectiveness objective has priority over the lifetime-aware objective in our system model, we set $\epsilon = 0.2$ to balance UAV battery lifetime while ensuring comprehensive UT service coverage.

Fig. 11(a) shows the trade-off between the lifetime-aware and effectiveness objectives for the GAT-based MADDPG algorithm across different coefficients φ . As φ increases from 0.2 to 0.3, there is a significant increase in the number of UTs

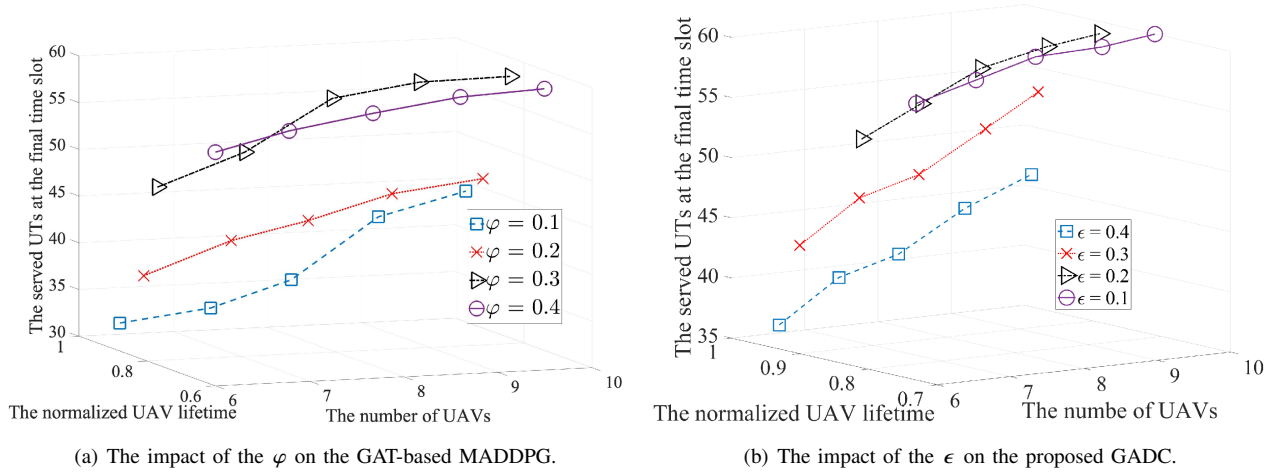


Fig. 11: The trade-off performance comparison between the GAT-based MADDPG and the proposed GADC.



Fig. 12: The deployment of UAVs when UTs are in an open area

served but a corresponding decline in lifetime. The impact becomes less pronounced as φ further increases from 0.3 to 0.4. These varying outcomes with different φ values highlight the importance of careful coefficient selection based on expert knowledge. Fig. 11(b) shows the influence of ϵ on the dual-objective optimization process. Increasing ϵ leads to improved UAV lifetime but decreased UT service coverage. Unlike φ 's influence shown in Fig. 11(a), ϵ 's impact appears more linear and predictable. Consequently, it is much easier for GADC to steer the tradeoff between the dual objectives by tuning ϵ .

B. Performance evaluation in the digital-twin simulator

In contrast to the obstacle-free ideal environment simulated in the last subsection, the digital twin environment models a realistic urban landscape based on Munich's 3D map. We employ ray tracing to accurately calculate the channel power between the UAVs and the UTs. In open areas, the LoS links predominates; however, within urban settings, the communication link is established through a complex interplay of multiple reflections and refractions. Consequently, we assess the proposed GADC and compare its performance against state-of-the-art algorithms. In the training phase, we configure the system with five UAVs and 40 UTs. The small number of UAVs and UTs during training is due to the substantial computational resources required for ray tracing calculations. In the subsequent testing phase, the system scales up to 10

UAVs and 60 UTs by using averaged weights and parameters from training models to create a new UAV control model.

Fig. 12 compares the UAV deployment across various algorithms when the UTs are located in an open area (square) in the city. The blue dots represent the UAVs, while the green dots represent the arbitrarily located UTs. Fig. 12(a) illustrates the initial random positions of the UTs and UAVs. Figs. 12(b) and 12(c) depict the final UAV deployments of the proposed GADC and the conventional MADDPG algorithms, respectively. The figures show that GADC achieves near-uniform UAV distribution above the UTs, while conventional MADDPG positions UAVs at the outer edges of the coverage area, farther from the central UT concentration. Such disparity arises because MADDPG-controlled UAVs cannot share local observations, limiting the UAVs' ability to detect areas with high UT density. Finally, since GAT-based MADDPG's final deployment performance closely resembles GADC's, its simulation results are omitted from this comparison for simplicity.

Fig. 13 illustrates the UAV deployment when some UTs are distributed in narrow streets and between buildings. In this context, some UTs are not able to establish direct links with the UAVs. They may have multiple reflections and refractions to achieve connectivity. Fig. 13(a) shows the initial positions of the UTs and UAVs, whereas Figs. 13(b) and 13(c) depict UAVs' deployment positions of the proposed GADC and MADDPG at the final time step, respectively. GADC-controlled UAVs maintain a clustered distribution, staying

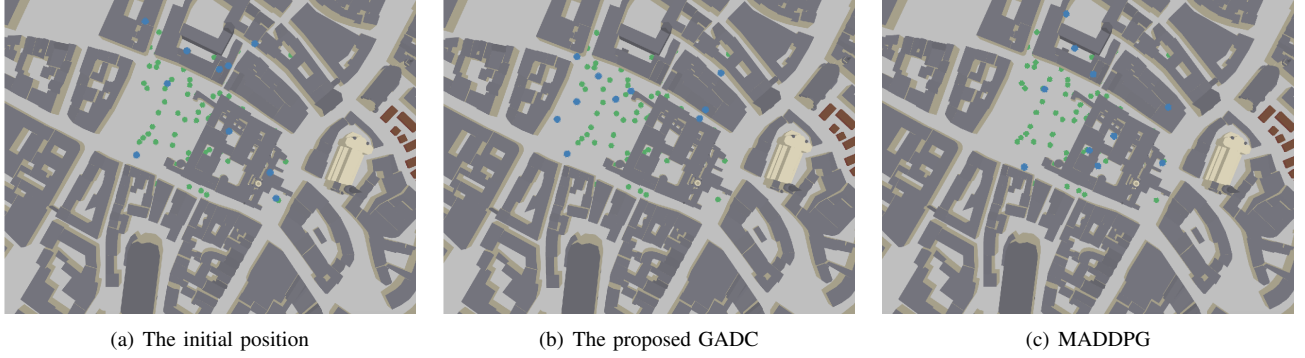


Fig. 13: The deployment of UAVs at the final step when in an urban scenario

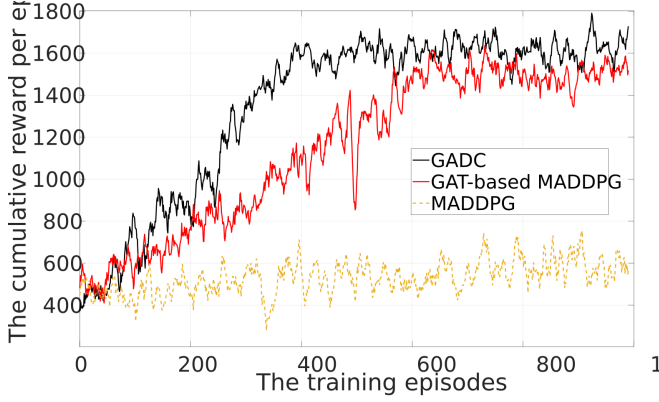


Fig. 14: The convergence performance of different algorithms in the NVIDIA Sionna simulator.

within the observation range of their nearest neighbors to maintain connectivity. In contrast, MADDPG-controlled UAVs show a dispersed distribution, with most UAVs positioned outside each other's communication range. This disparity stems from GAT's ability to enable UAVs to identify high UT density regions by aggregating observations from neighboring UAVs, allowing them to prioritize movement toward these densely populated areas.

As illustrated in Fig. 14, the proposed GADC significantly outperforms the benchmark algorithms in convergence speed. It achieves an episode reward ranging from 1,500 to 1,600 in approximately 400 episodes, whereas the GAT-based MADDPG requires about 600 episodes to achieve the same reward level. Note again that the proposed GADC optimizes the dual objectives independently, providing a more precise optimization trajectory to the weighted single-reward optimization. Moreover, the traditional MADDPG fails to converge and exhibits considerable fluctuations, as limited observations hinder the strategic optimization of distributed UAVs.

One may notice that both the proposed GADC and the GAT-based MADDPG converge faster in Fig. 14 than in Fig. 8. This improvement is due to the reduced scale during training (10 UAVs and 40 UTs, down from 20 UAVs and 120 UTs). The good testing performance in this subsection demonstrates the strong generalization capability of GAT-based learning, as systems trained at smaller scales can effectively scale up

to larger deployments. This implies good generalizability of GAT-based learning, which allows a system trained on a small scale to be generalized to one with a larger scale.

VI. CONCLUSIONS

This study focused on optimizing dual objectives in multi-UAV systems: maximizing user terminal (UT) coverage while extending UAV battery longevity. We developed the Graph Attention-based Decentralized Actor-Critic (GADC) method, which leverages Graph Attention Network layers to aggregate information from neighboring UAVs to efficiently explore unobserved areas. By implementing dual critics, the GADC achieves rapid convergence toward optimal solutions for both objectives independently. We tested the proposed scheme in NVIDIA Sionna, where the UAV-UT channels are generated by ray tracing. Numerical results demonstrate that GADC significantly improves both system lifetime and service coverage compared to existing approaches.

REFERENCES

- [1] Z. Ye, *et al.*, "Multi-UAV navigation for partially observable communication coverage by graph reinforcement learning," *IEEE Trans. Mob. Comput.*, vol. 22, no. 7, pp. 4056–4069, Jan. 2023.
- [2] Z. Yang, *et al.*, "Online trajectory and resource optimization for stochastic UAV-enabled MEC systems," *IEEE Trans. Wireless Commun.*, vol. 21, no. 7, pp. 5629–5643, Jul. 2022.
- [3] Y. Liu, *et al.*, "Fair and energy-efficient coverage optimization for UAV placement problem in the cellular network," *IEEE Trans. Commun.*, vol. 70, no. 6, pp. 4222–4235, Jun. 2022.
- [4] R. Madan, *et al.*, "Distributed algorithms for maximum lifetime routing in wireless sensor networks," *IEEE Trans. Wireless Commun.*, vol. 5, no. 8, pp. 2185–2193, Aug. 2006.
- [5] X. Zhang, *et al.*, "Cooperative trajectory design of multiple UAV base stations with heterogeneous graph neural networks," *IEEE Trans. Wireless Commun.*, vol. 22, no. 3, pp. 1495–1509, Mar. 2023.
- [6] J. Schulman, *et al.*, "Trust region policy optimization," in *Proc. the 32nd Int. Conf. Mach. Learn. (ICML)*, vol. 37, Lille, France, Jul. 2015, pp. 1889–1897.
- [7] —, "Proximal policy optimization algorithms," *arXiv preprint arXiv:1707.06347*, 2017.
- [8] H. Peng, *et al.*, "Energy harvesting reconfigurable intelligent surface for UAV based on robust deep reinforcement learning," *IEEE Trans. Wireless Commun.*, vol. 22, no. 10, pp. 6826–6838, Oct. 2023.
- [9] L. T. Hoang, *et al.*, "Deep reinforcement learning-based online resource management for UAV-assisted edge computing with dual connectivity," *IEEE/ACM Trans. Netw.*, vol. 31, no. 6, pp. 2761–2776, Dec. 2023.
- [10] C. Li, *et al.*, "Deep reinforcement learning-based mining task offloading scheme for intelligent connected vehicles in UAV-aided MEC," *ACM Trans. Des. Autom. Electron. Syst.*, vol. 29, no. 3, pp. 1–29, May 2024.

- [11] Z. Yang, *et al.*, “Dynamic offloading and trajectory control for UAV-enabled mobile edge computing system with energy harvesting devices,” *IEEE Trans. Wireless Commun.*, vol. 21, no. 12, pp. 10 515–10 528, Dec. 2022.
- [12] R. Liu, *et al.*, “Resource allocation for NOMA-enabled cognitive satellite-UAV-terrestrial networks with imperfect CSI,” *IEEE Trans. Cog. Commun. Netw.*, vol. 9, no. 4, pp. 963–976, Aug. 2023.
- [13] Y. Liu, *et al.*, “Space-air-ground integrated networks: Spherical stochastic geometry-based uplink connectivity analysis,” *IEEE J. Sel. Areas Commun.*, vol. 42, no. 5, pp. 1387–1402, May 2024.
- [14] Z. Yin, *et al.*, “UAV-assisted secure uplink communications in satellite-supported IoT: Secrecy fairness approach,” *IEEE Internet Things J.*, vol. 11, no. 4, pp. 6904–6915, Feb. 2024.
- [15] L. Zhou, *et al.*, “Intelligent UAV swarm cooperation for multiple targets tracking,” *IEEE Internet Things J.*, vol. 9, no. 1, pp. 743–754, Jan. 2022.
- [16] G. Raja, *et al.*, “Efficient and secured swarm pattern multi-UAV communication,” *IEEE Trans. Veh. Technol.*, vol. 70, no. 7, pp. 7050–7058, Jul. 2021.
- [17] C. H. Liu, *et al.*, “Energy-efficient UAV control for effective and fair communication coverage: A deep reinforcement learning approach,” *IEEE J. Sel. Areas Commun.*, vol. 36, no. 9, pp. 2059–2070, Sep. 2018.
- [18] Z. Feng, *et al.*, “Multi-agent reinforcement learning with policy clipping and average evaluation for UAV-assisted communication markov game,” *IEEE Trans. Intell. Transp. Syst.*, vol. 24, no. 12, pp. 14 281–14 293, Dec. 2023.
- [19] Y. Hou, *et al.*, “UAV swarm cooperative target search: A multi-agent reinforcement learning approach,” *IEEE Trans. Intell. Veh.*, vol. 9, no. 1, pp. 568–578, Jan. 2024.
- [20] S. Kakade, *et al.*, “Approximately optimal approximate reinforcement learning,” in *Proc. Int. Conf. Mach. Learn.*, San Francisco, CA, Jul. 2002, pp. 267–274.